Chapter 16

Interrogation of Nonadiabatic Molecular Dynamics via Time-Resolved Photoelectron Spectroscopy

Michael S. Schuurman and Albert Stolow

1. Introduction 634
2. Wavepacket Dynamics 636
2.1. Born–Oppenheimer wavepacket dynamics 636
2.2. Nonadiabatic wavepacket dynamics 641
2.3. Selection of experimental observables 644
3. Principles of Time-Resolved Photoelectron Spectroscopy 645
3.1. Photoelectron spectroscopy as a probe 645
3.2. Description of electronic and nuclear degrees of freedom 649
4. Applications of Time-Resolved Photoelectron Spectroscopy 657
4.1. Experimental demonstration of TRPES 657
4.2. Interrogation of molecular dynamics employing TRPES 660
5. Concluding Remarks 662
Acknowledgments 664
References 664

Steacie Institute for Molecular Sciences, National Research Council, Canada.

1. Introduction

The time evolution of photoexcited molecular systems invariably involves the complicated coupling of nuclear and electronic dynamics, resulting in a myriad of potential radiationless processes such as internal conversion, isomerization and proton transfer reactions.[1−8] The unambiguous elucidation of the photodynamics of polyatomic molecular systems will require a set of theoretical and experimental tools robust enough to disentangle these coupled dynamical processes.

The primary reason that dynamics in the excited states of molecules are, in general, qualitatively different from dynamics in the ground state, and correspondingly more complicated to study, is due to the frequent breakdown of the Born–Oppenheimer approximation (BOA) in these regimes. The BOA states, in part, that the electronic energy depends only parametrically on the nuclear coordinates.[9] The justification for this approximation lies in the different mass scales between the relatively heavy nuclei versus the lightweight electrons. In this picture, the electronic distribution relaxes instantaneously upon displacement of the nuclei, thereby defining the potential energy surfaces on which the nuclei move. The BOA, in the context of nuclear motion on a given electronic state, is also a statement about how energetically isolated a particular electronic state is from the manifold of all electronic states. A breakdown of the BOA occurs when the parametric dependence on the nuclei becomes a functional one, which will occur when electronic states come into close energetic proximity. In addition, and complimentarily, this situation is associated with a concomitant increase in the derivative coupling between the now energetically proximal electronic states. One understands the difference between this parametric and functional dependence intuitively given that when the BOA is valid, small nuclear perturbations generate small perturbations in the electronic energy, whereas in a region near an electronic degeneracy, small nuclear perturbations may result in qualitative changes in the electronic character of the nearby states.

It is because excited electronic states of polyatomic molecules generally occur in manifolds, as opposed to energetically well separated potential energy surfaces, that the breakdown of the BOA is a standard characteristic of excited state dynamics. A particularly relevant breakdown of the BOA occurs when two (or more) electronic states are degenerate at a given nuclear configuration. If the degeneracy of the electronic states is lifted linearly in the vicinity of this point via a specific set of nuclear

displacements, it is termed a conical intersection. For an intersection of two electronic states these nuclear displacements, in general, correspond to motion along exactly two coordinates which span the branching[10] or g-h space.[11] These directions are readily determined from *ab initio* gradient information, where the g direction is defined as the energy difference gradient between the two states, while the h direction is collinear with the nonadiabatic coupling gradient. Similarly, if nuclear motion is to be treated in terms of normal mode vibrations, generally only a subset of vibrational modes will be identified with nonadiabatic transitions and are termed tuning or coupling modes.[8,12] Analogous to the internal coordinate treatment, here the former identify those vibrational modes which affect the energy difference between the states of interest, while the latter is associated with of modulation the nonadiabatic coupling. Thus, passages through conical intersections that result in transitions from one electronic state to another are effectively described by only a small subset of vibrational modes/internal coordinates.

Conical intersections are extremely efficient at facilitating nonradiative transitions between electronic states, and when found in the Franck–Condon region, can lead to transitions between electronic states on femtosecond timescales following the absorption of the excitation photon. These theoretical concepts have proven useful in the characterization and simulation of nonadiabatic dynamics in molecular systems, but direct spectroscopic observation of passages through conical intersection, and nonadiabatic transitions in general, in polyatomic systems with many vibrational degrees of freedom remains a more significant challenge.

One experimental approach that has been developed to interrogate complex excited state dynamics is gas-phase time-resolved photoelectron spectroscopy (TRPES).[13−25] This pump-probe spectroscopic technique first prepares a non-stationary state on the excited state manifold, then employs a time-delayed ionizing probe laser pulse to determine photoelectron spectra as a function of time. Assuming the excited state potential energy surface differs from that of the ground state, the time-dependent evolution of the prepared wavepacket will necessarily involve nuclear motion, a process which may be observed in the evolution of the Franck–Condon spectra that define the vibrational structure of the bands in the photoelectron spectrum. If, however, the wavepacket undergoes a nonadiabatic transition to a different electronic state, one could expect a dramatic change in the dominant ionization channel which would be observed as a change in the kinetic energy spectrum of the emitted photoelectron. We note that the processes

we call *chemistry* involve the rearrangement of the valence (as opposed to inner shell) electrons, and therefore we expect that photoelectron spectroscopies (i.e. UV as opposed to X-ray) which are directly sensitive to the valence electrons will confer the greatest insights. Additionally, the photoelectron angular distribution, an information-rich observable that can be employed to help elucidate the electronic character of the ionized state, would also be expected to display a time dependence that is sensitive to electronic states on which the wavepacket is propagating.[26]

Thus, TRPES techniques have in principle the ability to detect both changes in the motion of the nuclei, as well as the evolution of the valence electronic structure of the time-dependent wavepacket. Some details of the method, and potential complications, will be discussed in further detail below. In this discussion, our language shall assume that the excited state dynamics occur on a manifold of neutral electronic states, which upon ionization yield a singly charged cationic species. While this is the simplest and most straightforward implementation of the technique, TRPES is of course not limited to these scenarios. In the following, we present in Sec. 2 the wavepacket formalism necessary for a conceptual understanding of the motivations and results of TRPES, while in Sec. 3 we discuss limiting pedagogical cases of molecular systems that may be studied using this technique. In Sec. 4 we present representative experimental applications, and we close with a prognosis for the future of the approach and the increasingly important interplay between theory and experiment.

2. Wavepacket Dynamics

2.1. *Born–Oppenheimer wavepacket dynamics*

In order to discuss the physical processes involved in the preparation of a molecular excited electronic state and the subsequent evolution of the nuclei on the corresponding potential energy surfaces, the most conceptually straightforward approach is to invoke the notion of time-dependent vibronic wave packets. A pump-probe experiment of the type considered here involves three distinct steps: the pump, in which ground state population is transferred to an excited state, the evolution of the excited state population, and finally, the probe, in which the excited state wavepacket is projected onto a manifold of final states.

Under this ansatz, the evolving non-stationary state is represented as a wavepacket, which is defined as a coherent superposition of

time-independent eigenstates:

$$|\psi(t)\rangle = \sum_{\alpha} C_{\alpha}(t)|\Psi_a\rangle, \tag{1}$$

where

$$C_{\alpha}(t) = A_{\alpha}e^{-iE_{\alpha}t/\hbar}. \tag{2}$$

As Eq. (2) shows, the coefficients $C_{\alpha}(t)$ are complex valued and time dependent. The initial phase and amplitude of the wavepacket component state α prepared by the pump laser pulse is contained in the complex-valued coefficient A_{α}. Since the exact eigenstate $|\Psi_{\alpha}\rangle$ is time-independent, the evolution of the wavepacket is wholly determined by the changes in the coefficients $C_{\alpha}(t)$.

During the probe process, the wavepacket is lifted up onto the manifold of final states, where the transition probability to a given final state $|\Psi_f\rangle$ is given by:

$$\begin{aligned} I_f(t;\omega) &= |\langle\Psi_f|E(\omega)\cdot\mu|\psi(t)\rangle|^2 \\ &= \left|\sum_{\alpha} A_{\alpha}\langle\Psi_f|E(\omega)\cdot\mu|\Psi_{\alpha}\rangle e^{-iE_{\alpha}t/\hbar}\right|^2 \\ &= \left|\sum_{\alpha} B_{\alpha}(\omega)e^{-iE_{\alpha}t/\hbar}\right|^2. \end{aligned} \tag{3}$$

If one expands the norm shown in Eq. (3), employing standard trigonometric identities, the resulting series can be expressed as a double sum:

$$I_f(t;\omega) = \sum_{\alpha,\beta} |B_{\alpha}||B_{\beta}|\cos([E_{\alpha} - E_{\beta}]t/\hbar + \Phi(\alpha,\beta)), \tag{4}$$

where $\Phi(\alpha,\beta)$ contains the phase difference between the $B_{\alpha,\beta}$ coefficients, each of which contain the initial phase of the component states, α and β, of the wavepacket and the phase of the transition dipole matrix elements connecting each state to the final state $|\Psi_f\rangle$. Figure 1 illustrates both the initial preparation of the excited state wavepacket, and the subsequent projection of this superposition of states onto a manifold of final states via a probe photon.

Since the time dependence in the observed transition intensity shown in Eq. (4) is multiplied by the energy difference $E_{\alpha} - E_{\beta}$, the total signal,

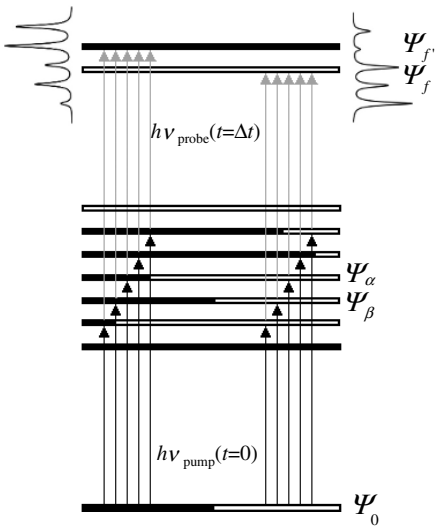

Fig. 1. Schematic for wavepacket creation and subsequent simultaneous projection onto a manifold of final states. Following excitation from the initial state ψ_0, the excited state wavepacket is composed of states (denoted ψ_α, ψ_β, etc.) with varying degrees of "black" and "white" character (for example, bond stretch and angle bend vibrational modes). The choice of final state, either "white" (ψ_f) or "black" ($\psi_{f'}$), will differentially project out different components of the wavepacket based on the degree of overlap between the two states.

shown to be a coherent sum of all interferences between pairs of states in the wavepacket, will display modulations at frequencies corresponding to all the level spacings present in the neutral state wavepacket. Therefore, the Fourier transform of the time-domain signal will yield a power spectrum in which energy level spacings within the prepared neutral state may be observed. However, the amplitude with which these frequencies appear in the transformed spectrum depends on the modulation depth of the signal, i.e. the amplitude is given by the product $|B_\alpha||B_\beta|$. From Eq. (3), one observes that the magnitude of $|B_\alpha|$ depends on the magnitude of the A_α, but more importantly, on the magnitude of the transition dipole matrix element between the neutral state Ψ_α with the final state Ψ_f. If the norm of these terms of is approximately equal, then the interference between the two transitions will be alternatively totally destructive or constructive, yielding a strong signal in the power spectrum at this frequency, with intensity proportional to these amplitudes. Conversely, if one of the amplitudes is small due to poor overlap with the final state (e.g. a forbidden transition),

the interference will be minimal and only a weak signal at the frequency corresponding to this level spacing would be expected.

Since, for the case of photoionization detection, it is likely that many final states will be accessible given the photon energy of the probe laser pulse, the probe step is actually the projection of the wavepacket onto numerous final states, each resulting in a distinct set of interferences. It is precisely this simultaneous projection onto multiple states in the cationic manifold that enables the characterization of the excited state wavepacket. If the characters of the final states in the projection are known, the wavepacket may be successfully probed based on the differential signal with each level. For example, Fig. 1 shows coherent two photon transitions in which the final state is either of "black" or "white" character. Each of these states exhibit favorable overlap with neutral states that are primarily of the same character, as evinced by the spectral profiles shown in the diagram. When coherent two-photon transitions to the final state of white character are considered, the resultant power spectrum will display strong signal corresponding to the level spacings between the predominantly white states of the neutral, while the converse will be true for the primarily black final state. The level spacings corresponding to eigenstates of mixed character will arise with varying intensities depending on the relative (and absolute) magnitudes of the overlap with the chosen final state. In this way, the final states onto which the wavepacket is projected are effectively *filters* through which components of the wavepacket may be viewed. Through a reasonable selection of final vibronic states onto which the projection is performed, both the electronic and nuclear character of the evolving excited state wavepacket may be successfully interrogated as a function of time.

While the exact non-Born–Oppenheimer eigenstates employed in Eq. (1) are of use for in a formal discussion of wavepacket dynamics, they are in practice seldom accessible. Instead, these exact states are expanded in a basis-set of known functions. These expansions, in addition to being necessary for a useful theoretical description and simulation of wavepacket dynamics, are also often of pedagogical utility, as the essential physics of the dynamical processes can be made more transparent.

To this end, we will begin by partitioning the total Hamiltonian of the system into a zeroth-order component and a perturbation, such that:

$$(H_0 + V)\Psi_\alpha = E_\alpha \Psi_\alpha. \tag{5}$$

The exact eigenstates, and thus the wavepacket defined in Eq. (1), may then be expressed in a perturbation theory expansion, where the zeroth-order

functions are those that diagonalize H_0. Employing the standard results of perturbation theory, one may obtain expressions for the energy of the system, such that:

$$H_0\big|\phi_\alpha^{(0)}\big\rangle = E_\alpha^{(0)}\big|\phi_\alpha^{(0)}\big\rangle, \tag{6}$$

$$E_\alpha = E_\alpha^{(0)} + E_\alpha^{\text{corr}} = E_\alpha^{(0)} + \big\langle\phi_\alpha^{(0)}\big|V\big|\phi_\alpha^{(0)}\big\rangle + \sum_{\beta\neq\alpha}\frac{\big|\big\langle\phi_\beta^{(0)}\big|V\big|\phi_\alpha^{(0)}\big\rangle\big|^2}{E_\beta^{(0)} - E_\alpha^{(0)}} + \cdots \tag{7}$$

$$\Psi_\alpha = \phi_\alpha^{(0)} + c_\alpha^{(1)}\phi_\alpha^{(1)} + c_\alpha^{(2)}\phi_\alpha^{(2)} + \cdots \tag{8}$$

Note that the second-order contribution to the perturbation energy is determined via coupling of zeroth-order states through the perturbation. Inserting these expressions into Eq. (1), one obtains

$$|\psi(t)\rangle = \sum_\alpha A_\alpha e^{-i\left(E_\alpha^{(0)}+E_\alpha^{\text{corr}}\right)t/\hbar}\phi_\alpha^{(0)} + \sum_\alpha C_\alpha(t)\sum_{n=1} c_\alpha^{(n)}\phi_\alpha^{(n)}. \tag{9}$$

If the perturbation, V, is small, then the first term in Eq. (9) will initially predominate and the short time behavior of the wavepacket will be well described by the zeroth-order states. However, it is precisely the coupling between zeroth-order states shown in Eq. (7), coupling that arises due to the terms excluded in the zeroth-order Hamiltonian, which give rise to time-evolution of the wavepacket in the zeroth-order basis.

To give a pedagogical example, a common choice for H_0 in molecular vibration problems is the harmonic oscillator Hamiltonian, which would result in the functions $\phi_\alpha^{(0)}$ being the normal modes of the system and the zeroth-order energies given by $E_i^{(0)} = h\omega_i(n_i + \frac{1}{2})$. However, the potential energy surfaces of molecular systems are to varying degrees anharmonic, which would be manifested in V containing cubic, quartic and higher-order potential terms. Additionally, many molecular systems, particularly those in excited electronic states, will display nonadiabatic transitions. The Hamiltonian for these systems will necessarily involve coupling between different electronic states, so that V may include the effect of coupling to other electronic states. The list of additional non-negligible potential couplings (i.e. spin-orbit, rotation-vibration, etc.) is virtually endless. Thus, the coupling between the zeroth-order states that arises due to the excluded terms in H_0 ensures that the states will evolve in time such that any initially prepared zeroth-order state will generally dephase into a complex superposition.

2.2. *Nonadiabatic wavepacket dynamics*

As discussed above, the initial preparation of an excited state wavepacket via a pump laser pulse creates a coherent superposition of states on the excited state manifold. Under the Born–Oppenheimer approximation,[9,27,28] the electronic energy is presumed to display only a parametric dependence (indicated by a semi-colon below) on the nuclear coordinates, $\mathbf{R}$, so that the electronic wavefunctions are given by:

$$H = T_e + V_e(\mathbf{r};\mathbf{R}) + T_N = H_e + T_N, \tag{10}$$

$$H_e\psi_e^i(\mathbf{r};\mathbf{R}) = E_e^i(\mathbf{R})\psi_e^i(\mathbf{r};\mathbf{R}), \tag{11}$$

where T_e and T_N are the electronic and nuclear kinetic energy operators, respectively, and V_e is the coulombic potential terms of the electrons and nuclei. If the total wavefunction is expanded in a zeroth-order basis in which the electronic component is described in terms of adiabatic electronic states, one obtains

$$\Psi_\alpha(\mathbf{r},\mathbf{R}) = \sum_i \chi_\alpha^i(\mathbf{R})\psi_e^i(\mathbf{r};\mathbf{R}). \tag{12}$$

Equation (12) is known as the Born–Huang expansion,[29] and the nuclear functions, $\chi_\alpha^i(\mathbf{R})$, may be viewed as the expansion coefficients. While Eq. (12) is formally exact, since the entire set of adiabatic electronic states form a complete basis, in practice the summation is truncated to include only the states of physical relevance to the molecular system under consideration.

In keeping with the discussion from the previous section, the time evolution of a wavepacket expanded in a basis of zeroth-order states is due to couplings between the basis functions, which in this case correspond to the Born–Oppenheimer states. One may construct a set of coupled equations for the expansion coefficients, $\chi_\alpha^i(\mathbf{R})$, by inserting the wavefunction expansion in Eq. (12) into the Schrödinger equation for the total system and left multiplying by $\psi_e^{j*}(\mathbf{r};\mathbf{R})$,

$$\sum_i \psi_e^{j*}(\mathbf{r};\mathbf{R})H_e\psi_e^i(\mathbf{r};\mathbf{R})\chi_\alpha^i(\mathbf{R}) + \sum_i \psi_e^{j*}(\mathbf{r};\mathbf{R})T_N\psi_e^i(\mathbf{r};\mathbf{R})\chi_\alpha^i(\mathbf{R})$$
$$= E_\alpha \sum_i \psi_e^{j*}(\mathbf{r};\mathbf{R})\psi_e^i(\mathbf{r};\mathbf{R})\chi_\alpha^i(\mathbf{R}), \tag{13}$$

followed by integration over the electronic coordinates:

$$E_e^j(\mathbf{R})\chi_\alpha^j(\mathbf{R}) + \sum_i \left\langle \psi_e^{j*}(\mathbf{r};\mathbf{R})\middle|T_N\middle|\psi_e^i(\mathbf{r};\mathbf{R})\right\rangle \chi_\alpha^i(\mathbf{R}) = E_\alpha\chi_\alpha^j(\mathbf{R}). \tag{14}$$

Since the nuclear kinetic energy is given by $T_N = -\frac{1}{2\mu}\nabla \cdot \nabla$, where μ is a reduced mass whose precise definition is coordinate system dependent, it is straightforward to obtain expressions for the matrix element in Eq. (14) given by:

$$\begin{aligned}\left\langle \psi_e^{j*}(\mathbf{r};\mathbf{R})\middle|T_N\middle|\psi_e^i(\mathbf{r};\mathbf{R})\right\rangle &= -\frac{1}{2\mu}(\delta_{ji}\nabla^2 + 2\mathbf{F}^{ji}\cdot\nabla + G_{ji}) \\ &= T_N\delta_{ji} - \mathbf{\Lambda}_{ji}. \end{aligned} \tag{15}$$

Finally, inserting Eq. (15) into Eq. (14), and converting to matrix notation yields

$$(\mathbf{T}_N + \mathbf{E}_e(\mathbf{R}) - \mathbf{\Lambda} - E_\alpha\mathbf{I})\boldsymbol{\chi}(\mathbf{R}) = \mathbf{0}, \tag{16}$$

where $\mathbf{T}_N$ and $\mathbf{E}_e(\mathbf{R})$ are diagonal matrices, with the elements of the latter given by the adiabatic electronic energies. Most germane to this discussion is the derivative coupling term, $\mathbf{\Lambda}$, which couples the adiabatic electronic states via the nuclear kinetic energy operator. The matrix elements that define of this term are given by

$$\begin{aligned}\mathbf{F}^{ji} &= \left\langle \psi_e^j(\mathbf{r},\mathbf{R})\middle|\nabla\psi_e^i(\mathbf{r},\mathbf{R})\right\rangle, \\ G^{ji} &= \left\langle \psi_e^j(\mathbf{r},\mathbf{R})\middle|\nabla^2\psi_e^i(\mathbf{r},\mathbf{R})\right\rangle. \end{aligned} \tag{17}$$

$\mathbf{F}^{ji}$ and G^{ji} are the first- and second-derivative couplings, respectively, where $\mathbf{F}^{ji}$ is a vector quantity whose length is determined by the number of nuclear degrees of freedom and G^{ji} is a scalar. Since the scalar couplings can be expressed as

$$\mathbf{G} = \nabla\cdot\mathbf{F} + \mathbf{F}\cdot\mathbf{F}, \tag{18}$$

the total nonadiabatic coupling term is fully determined by the $\mathbf{F}$ matrices, which will subsequently be denoted simply as the derivative coupling. The magnitude of $\mathbf{F}^{ji}$ can be considerable even at significant distances from a point of degeneracy.[30] If the gradient operator is applied to Eq. (11) for states i and j, one can show that $\mathbf{F}^{ji}$ is given by:

$$\mathbf{F}^{ji} = \frac{\left\langle \psi_e^j(\mathbf{r},\mathbf{R})\middle|\nabla H_e\middle|\psi_e^i(\mathbf{r},\mathbf{R})\right\rangle}{E_e^i - E_e^j}. \tag{19}$$

As implied by the energy difference denominator, this term becomes particularly large as the energy difference between states i and j becomes

small, and will be singular when the two electronic states are degenerate. If the degeneracy is lifted linearly (i.e. not due to the Renner–Teller effect),[31,32] the crossing between states i and j may be termed a conical intersection.

The computation of accurate electronic wavefunctions has been one of the primary foci of *ab initio* quantum chemistry over the past few decades. In particular, advances in the computation of analytic energy gradients and derivative couplings now allow for the efficient *ab initio* determination of the derivative coupling terms in Eq. (19), thus enabling the quantitative description of nonadiabatic processes in general, and points of conical intersection in particular.

In order to determine the electronic wavefunctions defined in Eq. (11), the adiabatic electronic states are expanded in a configuration state function (CSF) basis such that

$$\psi_e^i(\mathbf{r};\mathbf{R}) = \sum_{k=1}^{N^{CSF}} c_k^i(\mathbf{R})\phi_k(\mathbf{r};\mathbf{R}), \tag{20}$$

where $\phi_k(\mathbf{r};\mathbf{R})$are spin-adapted linear combinations of Slater determinants and $c_k^i(\mathbf{R})$ are the configuration interaction (CI) coefficients.[30,33,34] While the electronic structure aspects of the following discussion will assume CI type wavefunctions and will thus employ this nomenclature, it should be noted that equation-of-motion coupled cluster (EOM-CC) methods[35,36] are also being successfully employed, with increasing frequency, to study the influence of nonadiabatic processes on molecular dynamics.[37−39]

To illustrate the concepts introduced thus far, we close this section by considering the time evolution of a hypothetical wavepacket on a manifold of excited electronic states which display regions of strong nonadiabatic coupling. At time $t = 0$, following the creation of the wavepacket on an excited electronic state, the initial wavepacket is well represented by a single zeroth-order, adiabatic electronic state. The wavepacket will then evolve in time due to the motion of the nuclei, corresponding to the forces on the potential energy surface. At some later time, dependent on the topography of the potential energy surface on which the wavepacket is evolving, the wavepacket will approach a region in which the derivative coupling between the current adiabatic state and another state becomes large. This scenario is generally associated with a decrease in the energy difference between the two states. As the coupling increases, the total wavefunction can no longer be associated with a single zeroth-order state,

but is rather a linear combination of electronic states due to the mixing engendered by the (now large) derivative coupling terms. If the coupling is indeed strong, there is the possibility that the wavepacket will undergo a qualitative change in character, which can be uniquely identified as a transition to a different adiabatic electronic state. That is to say, as the wavepacket vacates the coupling region, it is now well represented by a different zeroth-order electronic state. The ability to describe and predict the nature of these changes in wavepacket character, as well as the time scales on which they occur, continues to be a growing area of modern research in theoretical/computational chemical physics. Employing spectroscopic methods to access this information, particularly in general cases for "large" molecules, presents a hosts of challenges.

2.3. *Selection of experimental observables*

To this point, we have not discussed the determination of any particular observables. Specifically, the nature of the process by which the wavepacket is projected onto a set of final states, i.e. the computation of an expectation value. The determination of an appropriate experimental observable is an important point not just for experimentalists, but for theorists as well. The simulation of molecular dynamics for chemically relevant molecular systems requires that a number of significant approximations be made at a number of levels. These include the level of rigour in the description of the electronic structure of the excited states, the number of nuclear degrees of freedom that will be explicitly considered, the degree to which nonadiabatic coupling is included, etc. Often these approximations are relatively trivial and can be easily justified and/or convincingly validated. However, they can just as often be motivated by computational efficacy or other concerns not related to the physics of the problem. As a result, multiple mechanistic pictures, or narratives, may be constructed for the same molecular system, depending on the approximations employed. The availability of experimentally determined observables, therefore, provides an invaluable constraint on the results of computational simulations. However, it should be noted that spectroscopically determined observables are of maximum utility when compared to independently computed observable quantities using theoretical methods, as opposed to direct comparisons to mechanistic narratives which may be consistent with multiple spectroscopic measurements.

The choice of observable employed to study these processes is a degree of freedom available to the investigator. The ultimate selection of an

observable must be motivated by the questions that one wishes to answer. In the case of interest here, the observable of choice should be sensitive to *both* the reorganization of electronic charge and the motion of the nuclei: the degrees of freedom relevant to the dynamics of the nonadiabatic process under investigation. Furthermore, the observable should be non-vanishing for the degrees of freedom being studied on the time scales of the experiment. If one were to employ electronic absorption spectroscopy to monitor the evolution of a vibronic wavepacket, possible changes in the relevant selection rules would have to be known and anticipated. For example, if the wavepacket were to undergo intersystem crossing, evolving from singlet to triplet character, the selection rules governing the allowed transitions would change drastically, leading to a drop off in signal (i.e. formation of the so-called "dark state"). In the absence of a measurable response, little could be said regarding the behavior of the wavepacket subsequent to the intersystem crossing.

In the section that follows, it is argued that the photoelectron spectrum is an observable of particular utility for studying nonadiabatic wavepacket dynamics on excited molecular electronic states. When measured on femtosecond timescales, time-resolved photoelectron spectroscopy offers insights into molecular dynamics with a level of detail that was once exclusively the domain of theoretical simulation.

3. Principles of Time-Resolved Photoelectron Spectroscopy

3.1. *Photoelectron spectroscopy as a probe*

The following discussion will argue that the energy resolved, angle integrated photoelectron spectrum is a simple but particularly powerful spectroscopic observable to employ in the study of excited state wavepacket dynamics. While even more information may be obtained from energy-angle-resolved spectra,[40] discussion of these techniques is beyond the scope of the present chapter and the interested reader is referred elsewhere for a more detailed treatment.[24,26,40–44] In addition to more conceptual concerns, any experimental probe of excited state dynamics should ideally have a number of practical characteristics. If the technique is to be applied to problems of broad chemical interest, it must be general enough to accommodate the countless complexities that define molecular systems, but sensitive enough to distinguish the often subtle differences in the

response of a time-evolving vibronic wavepacket. It is argued here that photoelectron spectroscopy is precisely such a multiplexed spectroscopic approach.

3.1.1. *Motivation*

Firstly, concerning the generality of the approach, there are no "dark states" in photoelectron spectroscopy, as ionization is practically always an allowed process. Treating the free electron as a spectator (an over-simplification), the intensity of a particular ionizing transition depends on the degree of overlap between the neutral and cationic state wavefunctions. This intensity may be described as a product of the overlap between the electronic wavefunctions and a Franck–Condon factor describing overlap of the vibrational component of the total wavefunction. The extent to which these factors can be considered independent enables the construction of experiments that are designed to disentangle nuclear and electronic degrees of freedom.

Secondly, the ability to unambiguously assign an observed spectrum to the molecular species that produces the signal (via the charge-to-mass ratio) is the signature of a powerful spectroscopic approach. The determination of a photoelectron spectrum involves not only the production of a photoelectron, the kinetic energy of which gives rise to the spectrum, but also a cationic molecular species that can be identified via mass spectrometry. If these spectra are measured in coincidence, the parent neutral source of the photoelectron spectrum can be uniquely identified. These photoelectron-photoion coincidence (PEPICO) experiments have proven successful in identifying the ion parent of a photoelectron spectrum in femtosecond resolved experiments.[45–47] Given the propensity of excited cationic states to fragment, the ability to differentiate parent ion signal from fragment ion signal is a significant advantage.

Furthermore, the presence multiphoton ionization processes, which can often obscure the nature of initially prepared wavepacket, as well as the identity of the ionized species, can be readily identified. Since the photoelectron spectrum is recorded at each time step, the kinetic energy of the emitted electron provides a decisive fingerprint for not only the final cationic channel the molecular species is ionized into, but also the total number of photons involved in the ionizing photon absorption process. Electrons generated via multiphoton process will be generally shifted to higher kinetic energies.

Many of these attractive features of a photoelectron spectroscopy probe of molecular dynamics are a result of employing a highly differential detection approach. Rather than measuring integrated quantities, such as ion yields, each measurement retains the energy resolution of the detected species. While the complications that arise in this approach may result in reduced signal levels, electron detection is nevertheless highly sensitive and amenable to data-intensive measurement of many photoelectron spectra.

3.1.2. *Description of photoionization*

The ionization of a polyatomic molecule during the probe step of a TRPES experiment involves the absorption of a photon in order to produce a cationic molecular species and a free electron (here treated as a spectator), where the kinetic energy of the latter is analyzed to construct the photoelectron spectrum. Assuming that the wavepacket at any time t corresponds largely to a particular zeroth-order state Ψ_0, then the matrix element that describes this projection at a given time on the cationic continuum state such that

$$I_f(t;\omega) \propto \left|\left\langle \Psi_f^{\text{cat}} \middle| \mu(\mathbf{r}) | \Psi_0 \right\rangle\right|^2. \tag{21}$$

It is common to represent the final cationic state as a spin-adapted, anti-symmetrized product of an $N-1$ electronic wavefunction with a single free electron wavefunction:

$$\begin{aligned}\Psi_f^{\text{cat}} = \frac{\left(1 - \sum_{i=1}^{N-1} \hat{P}_{iN}\right)}{\sqrt{2N}} \big(&\Psi_\alpha^{\text{cat}}(r_1, \ldots, r_{N-1})\phi_\beta(r_N) \\ &- \Psi_\beta^{\text{cat}}(r_1, \ldots, r_{N-1})\phi_\alpha(r_N)\big),\end{aligned} \tag{22}$$

where the subscripts α, β on Ψ^{cat} and ϕ indicate the spin of electrons r_{N-1} and r_N, respectively, and where the operator $\hat{P}_{iN}$ interchanges electrons i and N. Given this ansatz for the cationic wavefunction, and since the electrons are indistinguishable and the wavefunctions anti-symmetric, one may determine the photoelectron matrix element in Eq. (21) to be:

$$\begin{aligned}&\left|\left\langle \Psi_f^{\text{cat}} | \mu(r) | \Psi_0 \right\rangle\right| \\ &\quad = \sqrt{2N}\left[\begin{array}{l} \left\langle \phi_\beta(r_N) | \mu(r_N) \middle| \Psi_\alpha^{\text{cat}}(r_1, \ldots, r_{N-1})\Psi_0 \right\rangle \\ \qquad - \displaystyle\sum_{i=1}^{N-1} \left\langle \hat{P}_{iN}\Psi_\alpha^{\text{cat}}(r_1, \ldots, r_{N-1})\phi_\beta(r_N) \middle| \mu(r_N) | \Psi_0 \right\rangle \end{array}\right].\end{aligned} \tag{23}$$

The second term on the right-hand side of Eq. (23) will be non-zero when the free-electron function is not orthogonal to the neutral state wavefunction Ψ_0. In the case of photoionization, the overlap between the relatively localized neutral electronic state and the free electron will necessarily vanish in the asymptotic limit, an observation which is generally employed to justify a strong orthogonality approximation[48,49] and the corresponding neglect of this term.

The first term on the right-hand side of Eq. (23) contains the so-called Dyson orbital, defined as:

$$\phi_{fi}^{D}(r) = \sqrt{N} \int \Psi_f(r_1, \ldots, r_{N-1}) \Psi_i(r_1, \ldots, r_N) dr_1 \ldots dr_{N-1}, \qquad (24)$$

which when inserted into Eq. (23), in concert with strong orthogonality approximation, yields

$$\left\langle \Psi_f^{\text{cat}} \middle| \mu(r) \middle| \Psi_0 \right\rangle = \sqrt{2} \langle \phi_\beta(r_N) | \mu(r_N) \big| \phi_{f0}^{D}(r_N) \big\rangle. \qquad (25)$$

Note that the definition in Eq. (24) requires the identification of an initial neutral electronic state and a final cationic state, yielding a distinct Dyson orbital for each ionization channel. The quantitative calculation of these photoelectron matrix elements, as well as the analogous recombination matrix elements that simply interchange the definition of initial and final states, is an active area of research.[42,50–60] To rigorously address the scattering problems exemplified by the above expression often represents a significant computational challenge, particularly for molecules of chemical and/or biological interest.

The more modest goal of this chapter is to employ the above expressions in order to identify and anticipate the preferred ionization continuum for a given molecular system. In particular, the current discussion is primarily interested with the *relative* rates of ionization into different cationic electronic states from neutral state vibronic wavepackets. Thus, it is the relative norms of the Dyson orbitals that yield qualitatively accurate insights into the preferred ionization channels for wavepackets on a given electronic state to specific states of the cation.

While the measured photoionization signal will be dependent on the degree of overlap between electronic states of the neutral species and the energetically accessible electronic states of the cation, it will also be sensitive to changes in the vibrational character of the time-evolving wavepacket. As the wavepacket moves upon a single electronic potential energy surface,

the nuclear motion that characterizes the kinetic energy of the wavepacket will influence the Franck–Condon spectra that determine the vibrational structure of the observed photoelectron bands. In summary, the observed photoionization signal will be sensitive not only to the electronic character of the evolving wavepacket, via the overlap of the electronic wavefunction of the neutral species with the accessible ionization continua, but also to nuclear motion through the evolution of the Franck–Condon spectrum. As discussed above, it is this ability to experimentally monitor precisely these characteristics of the evolving wavepacket that makes photoelectron spectroscopy particularly well suited for the study of nonadiabatic dynamics in polyatomic molecules. The utilization of these sensitivities to elucidate dynamical processes, as well as the interpretation of the resultant spectra, will be discussed in more detail below.

3.2. *Description of electronic and nuclear degrees of freedom*

In the preceding sections, it has been shown that the degree to which particular final states in a photoelectron spectroscopy experiment view the character of a time-evolving wavepacket is defined by the projection of the wavepacket onto the set of accessible states in the molecular ionization continuum. In practice, the observed signal from a time-resolved photoelectron spectroscopy experiment can be interpreted in terms of contributions from electronic and vibrational scaling factors. Specifically, the ability to ionize a neutral excited state of a molecule on which a nuclear wavepacket is evolving depends on the final and initial electronic states as well as the vibrational character of the wavepacket and the energetically accessible vibronic levels in the cationic manifold.

Turning first to the electronic scale factor, this term is determined by the degree of overlap between the neutral electronic state and the cationic core to which the molecule is ionized. This overlap is quantified via the computation of Dyson orbitals and photoionization cross sections, as discussed above; the tendency of particular neutral electronic states to ionize to specific electronic states of the cation can be readily understood in terms of simple Koopmans' correlations.[61,62]

The Koopmans' approximation states simply that the first ionization energy of a molecule is equal to negative the orbital energy of the ionized electron. This approximation assumes that there is no orbital relaxation in the cationic manifold, and thus the same set of orbitals that define

the initial state wavefunction are employed in the description of the final cationic state. What the approximation implies is that photoionization occurs most efficiently when it is a one-photon, one-electron process. This simple picture of photoionization is a valuable pedagogical tool for understanding why molecules will preferentially ionize into different cationic continuum channels. For example, it is possible that the removal of an electron from the highest occupied molecular orbital (HOMO) of a neutral molecular species will produce an ionic core with an electronic configuration differing from the corresponding neutral only in the electron hole created left in the HOMO. These two states would be termed Koopmans' correlated and the ionization probability would be predicted to be high. In contrast, a neutral electronic configuration in which both HOMO electrons are promoted to the lowest unoccupied orbital (LUMO) would be predicted to be poorly correlated to the same cationic state, as removal of a single from the frontier orbital would produce an excited cationic electronic configuration. Following the seminal work of Domcke,[61] this interplay, and at times competition, between the electronic and vibrational correlation factors will be explored below employing a series of test cases that illustrate a wide range of behaviors.

3.2.1. *Complementary Koopmans' correlations (Type I)*

For time-resolved experiments involving nonadiabatic transitions between multiple excited states of the neutral species, the evolution of the electronic dynamics can be readily monitored if the different electronic states preferentially ionize to different states of the corresponding cation. Under these favorable circumstances, the different excited states under investigation can be said to display complementary ionization correlations. In this situation, the kinetic energy of the departing electron will generally be uniquely assigned to a particular cationic manifold, assuming the energy differences between the electronic states of the cation accessible by the probe photon energy are large enough to be distinguished. Figure 2 presents a schematic of an experiment of this type, in which the time-scale of nonadiabatic passage from one electronic state to another in uniquely correlated with a switch in dominant ionization channel, resulting in a sudden change in the kinetic energy spectrum of the photoelectrons.

Paradigmatic examples of such molecular systems are the linear polyenes.[63] The ten carbon chain decatetraene (DT), in particular, was the subject of TRPES studies.[64] The lowest-lying singlet excited states of

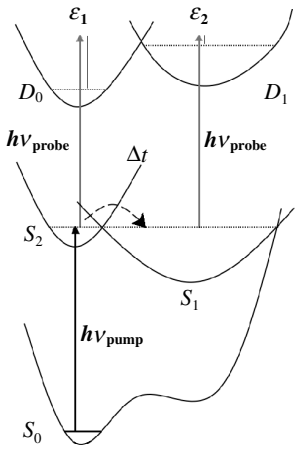

Fig. 2. A prototypical TRPES experiment in which a wavepacket is initially created at time $t = 0$ on state S_2, which preferentially ionizes to state D_0. The wavepacket evolves on this excited state for a time Δt, at which point it undergoes a nonadiabatic transition to state S_1. However, this electronic state preferentially ionizes to cationic state D_1, resulting in a change in the threshold ionization energy, from ε_1 to ε_2.

DT are identified as a bright S_2 state, accessed via a $\pi\pi^*$ transition, and an optically dark S_1 state, which can be excited directly in the Franck-Condon region only via multiphoton processes. As Table 1 shows,[65,66] the electronic structure of these two states is significantly different, with the S_2 state arising from a HOMO–LUMO transition, while the S_1 state involves double excitations out of the closed shell ground state. As such, each state correlates predominantly to a different electronic state in the cationic manifold. The first ionization threshold for the S_2 state corresponds to removal of the π^* electron, yielding the ground state of the cation, D_0. Conversely, ionization of the S_1 will preferentially form the first excited state of the cation, D_1.

If the Type I Koopmans' correlation picture provides a reasonable context for understanding TRPES measurements, once would expect a sudden switch in ionization channels as the vibronic wave packet undergoes a nonadiabatic transition from S_2 to S_1. Given that the excitation energy from D_0 to D_1 is approximately 1.5 eV, these transitions would correspond to a sudden decrease in the kinetic energy of the ejected photoelectrons of approximately the same magnitude and thus a shift of the photoelectron spectrum to lower energies. As Fig. 3 shows, this is indeed what is observed.

Table 1. Predominant molecular orbital configurations for the low-lying neutral and cationic electronic states of all-trans 2,4,6,8-decatetraene. The rightmost column indicates the Koopmans' correlated cationic state for each neutral configuration, assuming a single-photon, single-electron ionization event.

Electronic state	Energy (eV)	Molecular orbital occupancy					Weight[a]	Correlated state
		$1b_g$	$2a_u$	$2b_g$	$3a_u$	$3b_g$		
				Neutral				
S_0, $1\,^1A_g$	0.0	2	2	2	0	0	89%	D_0
S_1, $2\,^1A_g$	3.6	2	2	0	2	0	35%	D_1, D_2
		2	1	2	1	0	19%	D_1, D_2
		2	2	1	0	1	19%	D_0
S_2, $1\,^1B_u$	4.3	2	2	1	1	0	95%	D_0
				Cation				
D_0, $1\,^2B_g$	7.3	2	2	1	0	0	96%	
D_1, $1\,^2A_u$	8.7	2	1	2	0	0	53%	
		2	2	0	1	0	41%	
D_2, $2\,^2A_u$	9.6	2	1	2	0	0	38%	
		2	2	0	1	0	43%	
D_3, $2\,^2B_g$	9.7	1	2	2	0	0	56%	
		2	2	0	0	1	20%	

[a]Configuration weights computed employing semi-empirical QCFF/PI + CISD level of theory (Ref. 55).

The decrease in signal due to ionization of S_2 can be fit to exponential decay functions in order to determine a lifetime of the S_2 state of 402 ± 65 fs. The nonadiabatic transitions that give rise to the sub-picosecond excited state lifetimes, like those observed for DT, are very often facilitated by passage through seams of conical intersection.

3.2.2. *Corresponding Koopmans' correlations (Type II)*

While decatetraene is a limiting case for Type I (complementary) ionization correlations, many molecular systems will involve excited state dynamics where multiple electronic states will correlate to the same state of the cation. In these cases, the evolution of the vibronic wavepacket may not be readily disentangled on the basis of the kinetic energy of the ionized electron alone. When multiple electronic states of the neutral preferentially ionize to the same cationic state, they may be said to display corresponding ionization correlations (Type II).

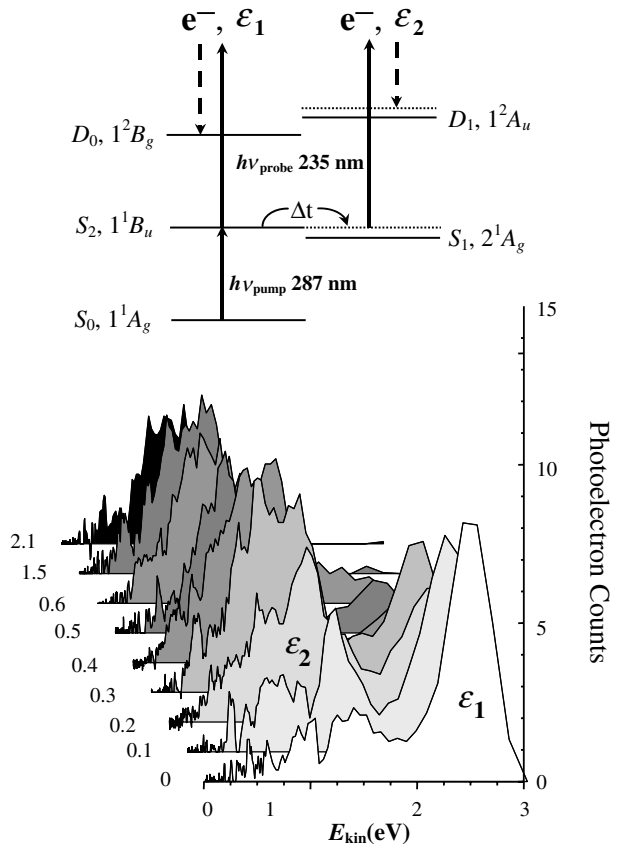

Fig. 3. (Top) Energy level scheme for TRPES of all-trans decatetratene, an example of a Type I molecule. The pump laser prepares the optically bright state S_2. Due to ultrafast internal conversion, this state converts to the lower lying state S_1 with $\sim 0.7\,\text{eV}$ of vibrational energy. The expected complementary Type I Koopmans' correlations are shown: $S_2 \rightarrow D_0 + \text{e}^-(\varepsilon_1)$ and $S_1 \rightarrow D_1 + \text{e}^-(\varepsilon_2)$. (Bottom) TRPES spectra of DT pumped at 287 nm and probed at 235 nm. There is a rapid shift ($\sim 400\,\text{fs}$) from ε_1, an energetic band at 2.5 eV due to photoionization of S_2 into the D_0 cation ground electronic state, to ε_2, a broad, structured band at lower energies due to photoionization of vibrationally hot S_1 into the D_1 cation first excited electronic state. The structure in the low energy band reflects the vibrational dynamics in S_1.

An example of such Type II systems can be found in the spectroscopic studies on the naphthalene and phenanthrene,[67] two rigid, fused ring molecular systems. As elucidated in Table 2, the leading electronic configurations of the pertinent excited states S_1 and S_2 have reasonable

Table 2. Predominant molecular orbital configurations for the low-lying neutral and cationic electronic states of phenanthrene. The rightmost column indicates the Koopmans' correlated cationic state for each neutral configuration, assuming a single-photon, single-electron ionization event.

Electronic state	Energy (eV)	Molecular orbital occupancy					Weight[a]	Correlated state
		a_2	a_2	b_1	a_2	b_1		
				Neutral				
S_0, $1\,^1A_1$	0.0	2	2	2	0	0	100%	D_0
S_1, $2\,^1A_1$	3.6	2	2	1	0	1	50%	D_0
		2	1	2	1	0	50%	D_1
S_2, $1\,^1B_2$	4.4	2	2	1	1	0	75%	D_0
		2	1	2	0	1	25%	D_1
				Cation				
D_0, $1\,^2B_1$	7.9	2	2	1	0	0	100%	
D_1, $1\,^2A_2$	8.4	2	1	2	0	0	100%	
D_2, $2\,^2A_2$	9.3	1	2	2	0	0	100%	

[a]Configuration weights computed employing semi-empirical QCFF/PI + CISD level of theory (Ref. 58).

overlap with the energetically accessible D_0 and D_1. Thus, one may expect to observe four different spectral bands in the photoelectron spectrum corresponding to ionization to the lowest two cationic states from both singlet excited states.

As Fig. 4 shows, there is a large degree of overlap between the observed ionization bands. However, the rigidity of the fused ring structures ensures that geometric changes between the ground, excited and cationic states are relatively small, thereby limiting the extent of vibrational progressions and ensuring that the $\Delta\nu = 0$ peak will dominate the photoelectron spectrum. Thus, the band origin of the $D_0 \leftarrow S_2$ ionizing transition, and its subsequent decay as a function of time, is clearly visible amongst the overlapping bands.

These same features of the potential energy surfaces aid in the identification of the rise in signal due to the ionization of S_1 state population. The adiabatic energy difference between the S_1 and S_2 states is approximately 0.75 eV. Thus, in order for population to transfer nonadiabatically from S_2 to S_1, the most favorable overlap of states will result in the creation of a wavepacket on S_1 with approximately 0.75 eV of vibrational energy. Since this vibrational energy should be largely conserved upon ionization to D_0, the S_1 ionization band should be shifted by the above amount relative to the S_2 ionization band, even though both neutral states ionize to the

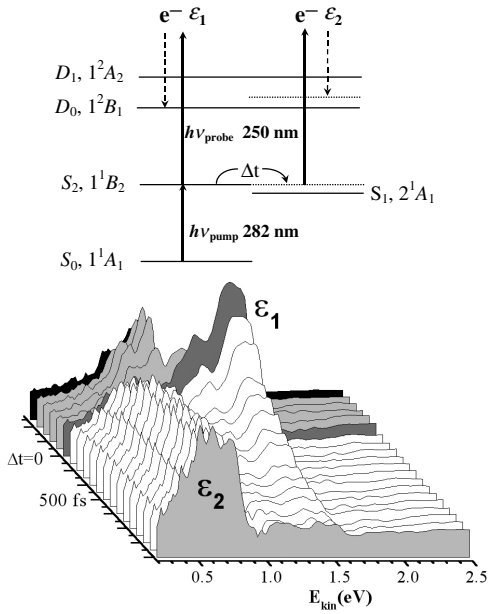

Fig. 4. (Top) Energy level scheme for TRPES of phenanthrene, an example of a Type II molecule. The pump laser prepares the optically bright state S_2. Due to ultrafast internal conversion, this state converts to the lower lying state S_1 with $\sim 0.74\,\text{eV}$ of vibrational energy. The expected corresponding Type II Koopmans' correlations are shown: $S_2 \rightarrow D_0 + \text{e}^-(\varepsilon_1)$ and $S_1 \rightarrow D_0 + \text{e}^-(\varepsilon_2)$. (Bottom) TRPES spectra of phenanthrene for a pump wavelength of 282 nm and a probe wavelength of 250 nm. The disappearance of band ε_1 at $\sim 1.5\,\text{eV}$ and growth of band at ε_2 at $\sim 0.5\,\text{eV}$ is a direct measure of the S_2–S_1 internal conversion time (520 fs). Despite the unfavorable Type II correlation, the rigidity of this molecule allows for direct observation of the internal conversion via vibrational propensities alone.

same cationic state. This is what is observed and an exponential fit of the decay of the S_2 state yields an excited state lifetime of $522 \pm 16\,\text{fs}$.

In this case it was possible to take advantage of the specifics of the molecular system in order to effective analyze the energy domain photoelectron spectra to observe the nonadiabatic transfer of electronic population and determine excited state lifetimes. However, it is straightforward to envision situations in which multiple excited states ionize to the same manifold of cationic states, or overlapping complementary Koopmans' correlated ionization channels. In these cases, an analysis of the photoelectron angular distributions may offer further information regarding the evolving electronic character of excited state vibronic wavepacket.

3.2.3. *Franck–Condon Spectra*

While the above sections have addressed the ability of photoelectron spectroscopy to monitor changes in the electronic character of excited state wavepackets, the evolution of the nuclear component of the wavepacket on a particular potential energy surface can also be tracked via changes in the vibrational structure of the corresponding photoelectron band. Clearly, it is the overlap of the vibrational component of the wavepacket with the energetically accessible vibrational levels of the cation that determines the appearance of this spectrum.

If the vibrational component of the excited state wavepacket is expanded in a basis of eigenfunctions of the harmonic oscillator Hamiltonian, than the nuclear motion is at zeroth-order is described by motion along a set of normal mode coordinates. The total vibrational wavefunction will then be a direct product of harmonic oscillator functions and the Franck–Condon factor is given by

$$d_{m,n} = \left\langle \prod_{i=1}^{N^{\text{vib}}} \chi_{m_i}^{\text{cation}}(Q_i) \middle| \prod_{j=1}^{N^{\text{vib}}} \chi_{n_j}^{\text{neutral}}(Q_j) \right\rangle, \tag{26}$$

where the harmonic oscillator eigenfunctions are defined by

$$\chi_i^j(Q_j) = \frac{1}{2^i i!} \left(\frac{\omega_j}{\pi}\right)^{\frac{1}{4}} H_i(\sqrt{\omega_j} Q_j) e^{-\omega_j Q_j^2/2}, \tag{27}$$

and ω_j are the harmonic frequencies associated with normal mode Q_j, and $H_i(x)$ are the Hermite polynomials of degree i. The efficient evaluation of these integrals are discussed elsewhere, including this current volume.[68–70] From the definitions above, these intensity factors are seen to be functions of the nuclear coordinates only. As the wavepacket evolves on an electronic state, its motion governed by the local energy gradients on potential energy surfaces, there will be a complementary reorganization of the nuclear coordinates which the Franck–Condon overlap integrals will be sensitive to. The schematic given in Fig. 1 can be readily applied to illustrate the simultaneous projection of the neutral excited state wavepacket onto a manifold of cationic vibrational energy levels. For example, one may associate the "white" and "black" states shown in the figure with bond stretch and angle bend vibrational energy levels, respectively, of the neutral and cation. If, at some initial time, the vibrational component of the wavepacket wavefunction is well described by a normal mode that is predominantly of bond stretch character, then observed Franck–Condon spectrum will

be largely due to those cationic vibronic energy levels that project out bond stretch modes, i.e. have large Franck–Condon overlap with bond stretching normal modes. As the wavepacket evolves and vibrational energy is redistributed to other modes via IVR (intramolecular vibrational energy redistribution) processes, one may observe that at some later time the vibrational wavefunction resembles an angle bend normal mode. The Franck–Condon spectrum would reflect this evolution, as the observed signal could now be assigned largely to the angle bend vibrational levels in the cation manifold.

In summary, the intensity of the time-dependent energy-resolved angle-integrated photoelectron spectrum can be approximated as the product of two scaling factors: the electronic transition dipole matrix element connecting the neutral excited state to the cationic continuum state, and the vibrational Franck–Condon factor. The latter is the basis for the projection of the vibrational component of the wavepacket onto the vibronic manifold of the cation, thereby giving rise to the vibrational structure of a given ionization band. The ability to project both the electronic and nuclear components of the wavepacket enables, in favorable cases, the disentanglement of these degrees of freedom, thereby simplifying the analysis of information rich spectral measurements.

4. Applications of Time-Resolved Photoelectron Spectroscopy

4.1. *Experimental demonstration of TRPES*

We have argued that TRPES could be an interesting method for studying excited state nonadiabatic processes in polyatomic molecules. By choosing observables obtained from photoionization, we expect to extract information about both charge and vibrational energy flow, and their coupling, during these ultrafast dynamical processes. Ultimately, however, the theoretically motivated ideas discussed above must be corroborated by experiment. In the following, we present experimental demonstrations, using femtosecond laser pulses in a pump-probe scheme with energy-resolved photoelectron detection, of the two limiting cases of Koopmans' correlations for TRPES.

An illustration of Type I Koopmans' correlations is ultrafast internal conversion in the linear polyene *all-trans* 2,4,6,8 decatetraene (DT). The first optically allowed transition in DT is $(S_2)\ 1^1B_u \leftarrow (S_0)\ 1^1A_g$. As

discussed above, the S_2 state is a singly excited configuration. In contrast, the lowest excited state is the dipole forbidden $(S_1)^1A_g$ state which arises from configuration interaction between singly and doubly excited A_g configurations. Nonadiabatic vibronic coupling, promoted by b_u symmetry vibrational motions, leads to ultrafast internal conversion from S_2 to S_1. As discussed above, the S_2 excited state electronically correlates with the (D_0) $1\ ^2B_g$ ground electronic state of the cation whereas the S_1 state correlates predominately with the (D_1) $1\ ^2A_u$ first excited state of the cation. Therefore, DT is an example of a Type I Koopmans' correlation.[63]

In Fig. 3 (top) we show the DT energy level scheme. A femtosecond pump pulse at 287 nm (4.32 eV) prepared the excited S_2 state in its vibrationless electronic origin. It then evolves into a vibrationally hot (~ 0.7 eV) S_1 electronic state via internal conversion. The rapidly evolving electronic states are observed by projecting the wavepacket onto several cation electronic states using a UV probe photon of sufficient energy (here, 235 nm, 5.27 eV). As discussed above, the nonadiabatic coupling evolves the electronic character of the wavepacket, switching the photoionization electronic channel. This, in turn, leads to large shifts in the time-resolved photoelectron spectrum. Indeed, the experimental photoelectron kinetic energy spectra in Fig. 3 (bottom) show a rapid shift from a narrow high energy band ($\varepsilon_1 = 2.5$ eV) to a broad, structured low energy band (ε_2). This is the direct observation of the evolving electronic character induced by nonadiabatic coupling: the 2.5 eV band is due to ionization of S_2 into the D_0 ion state; the broad, low energy band arises from photoionization of S_1 into the D_1 ion state. Integration of the two photoelectron bands directly reveals the S_2 to S_1 internal conversion time scale of 386 ± 65 fs. Furthermore, the vibrational structure within each photoelectron band yields information about the vibrational dynamics which promote and tune the electronic population transfer.

We now consider Type II Koopmans' correlations where such a favorable separation of electronic from vibrational dynamics might not be expected. Examples of Type II systems include the polyaromatic hydrocarbons, a specific example being S_2–S_1 internal conversion in phenanthrene (PH). In the case of PH, Table 2 shows that both the S_2 and the S_1 states correlate similarly with the electronic ground state as well as the first excited state of the cation.[67]

In PH, the nonadiabatic coupling of the bright electronic state (S_2) with the dense manifold of zeroth order S_1 vibronic levels leads to the

non-radiative "decay" (dephasing) of the zeroth order S_2 state. The energy gap between these two excited states is large and the density of S_1 vibronic levels is extremely large compared to the reciprocal electronic energy spacing. In this case, the dark state forms an apparently smooth quasicontinuum, the so-called statistical limit of the radiationless transition problem. The statistical limit is phenomenologically characterized by Lorentzian absorption bands where the apparent homogeneous width Γ is related to the apparent 'lifetime' of the bright state, $\tau \sim \hbar/\Gamma$.

We turn now to the femtosecond pump-probe photoelectron probing of excited state dynamics in PH. As illustrated in Fig. 4 (top), we excited PH from the $S_0\ ^1A_1$ ground state to the origin of the $S_2\ ^1B_2$ state with a 282 nm (4.37 eV) fs pump pulse. The excited molecules are then ionized after a time delay Δt using a 250 nm (4.96 eV) probe photon. The $S_2\ ^1B_2$ state rapidly internally converts to the lower lying $S_1\ ^1A_1$ state at 3.63 eV, transforming electronic into vibrational energy. In PH, both the $S_2\ ^1B_2$ and $S_1\ ^1A_1$ states correlate with the $D_0\ ^2B_1$ ion ground state, producing the ε_1 and ε_2 photoelectron bands. In Fig. 4 (bottom) we show time-resolved photoelectron spectra for PH, revealing a rapidly decaying but energetically narrow peak at $\varepsilon_1 \sim 1.5$ eV, due to photoionization of the vibrationless $S_2\ ^1B_2$ state into the ionic ground state $D_0\ ^2B_1$, with a decay time constant of 522 ± 16 fs. The broad band, centered at about ~ 0.7 eV is due to ionization of vibrationally hot molecules in the S_1 state, formed by the $S_2 - S_1$ internal conversion. At times $t > 1500$ fs or so (i.e. after internal conversion), the photoelectron spectrum is exclusively due to S_1 ionization, the S_1 state itself being long lived on the time scale of the experiment. Despite the fact that Type II molecules present an unfavorable case for disentangling electronic from vibrational dynamics, we can still see in PH a dramatic shift in the photoelectron spectrum as a function of time. This is due to the fact that PH is a rigid molecule and the S_2, S_1 and D_0 states all have similar geometries. The photoionization probabilities are therefore expected to be dominated by small Δv transitions. Hence, the 0.74 eV of vibrational energy in the populated S_1 state should be roughly conserved upon ionization into the D_0 ionic state. In PH, the small geometry change favors conservation of vibrational energy upon ionization, permitting the observation of the excited state electronic population dynamics. More generally, however, significant geometry changes will lead to overlapping photoelectron bands, complicating the disentangling of vibrational from electronic dynamics.

4.2. *Interrogation of molecular dynamics employing TRPES*

4.2.1. *Excited state intramolecular proton transfer*

Proton transfer is one of the most important chemical processes. Of interest here, excited state intramolecular proton transfer (ESIPT) processes are of particular importance since they allow for a detailed comparison of experiment with theory. *o*-hydroxybenzaldehyde (OHBA) is the smallest aromatic molecule displaying ESIPT. We used TRPES to study ESIPT in OHBA, the monodeuterated ODBA and the analogous two-ring system hydroxyacetonaphthone (HAN) as a function of pump laser wavelength, tuning over the entire enol $S_1(\pi\pi^*)$ absorption.[67]

In Fig. 5 (left), we show the energetics of OHBA. Excitation with a tunable pump laser $h\nu_{pump}$ forms the enol tautomer in the $S_1(\pi\pi^*)$ state. ESIPT leads to ultrafast population transfer from the S_1 enol to the S_1 keto tautomer. On a longer time scale, the S_1 keto population decays via internal conversion back to the ground state. Both the enol and keto excited state populations are probed by photoionization with laser $h\nu_{probe}$, producing the two photoelectron bands ε_1 and ε_2. In Fig. 5 (right), we present TRPES spectra of OHBA at an excitation wavelength of 326 nm, showing the two photoelectron bands ε_1 and ε_2. Band ε_1 is due to photoionization of the initially populated S_1 enol tautomer, band ε_2 to the photoionization of the S_1 keto tautomer. Both bands were observed across the whole absorption range (286–346 nm) of the S_1 state.

The decay of band ε_1 corresponds to the decay of the S_1 enol population and contains information about the proton transfer dynamics, with an estimated upper limit of 50 fs for the lifetime of the S_1 enol tautomer. Proton transfer reactions often proceed via tunnelling of the proton through a barrier and deuteration of the transferred proton should then significantly prolong the lifetime of the S_1 enol tautomer. In experiments with ODBA, we did not observe an isotope effect — i.e. the ESIPT reaction was again finished within 50 fs, showing that the barrier in the OH stretch coordinate must be very small or non-existent. TRPES also reveals the dynamics on the "dark" state, the S_1 keto state. The picosecond decay of band ε_2 corresponds to the loss of the S_1 keto population due to internal conversion to the ground state. The wavelength-dependent S_1 keto internal conversion rates in OHBA and ODBA likewise revealed no significant isotope effect. The measured internal conversion rates are very fast (1.6–6 ps over the range 286–346 nm) considering the large energy gap of 3.2 eV between

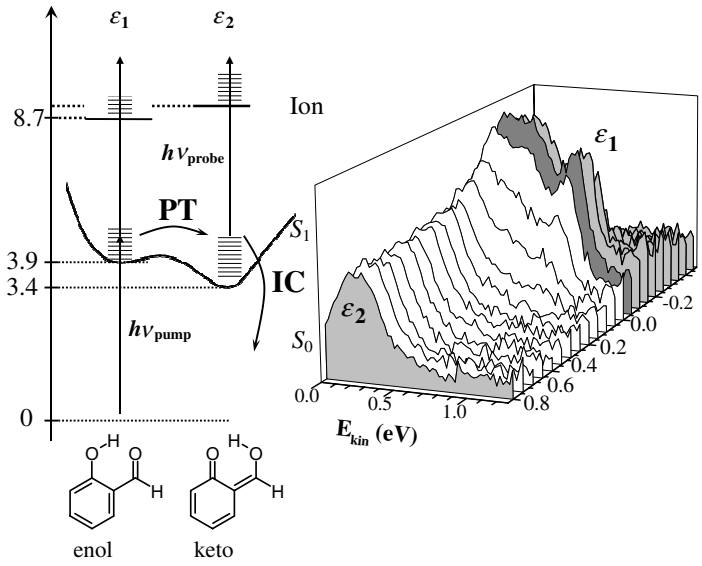

Fig. 5. (Left) Energetics for excited state proton transfer in OHBA, showing the enol and keto forms. Excitation with a pump laser E_{pump} forms the enol tautomer in the $S_1(\pi\pi^*)$ state. ESIPT leads to ultrafast population transfer from the S_1 enol to the S_1 keto tautomer. On a longer time scale, the keto S_1 population decays via internal conversion to the keto ground state. Both the enol and keto excited state populations are probed via ionization with a probe laser E_{probe}, producing the two photoelectron bands ε_1 and ε_2. (Right) TRPES spectra of OHBA at an excitation wavelength of 326 nm and a probe laser wavelength of 207 nm. Two photoelectron bands were observed: ε_1 due to ionization of the S_1 enol; ε_2 due to ionization of the S_1 keto. Band ε_1 indicates a sub-50 fs timescale for the proton transfer. Band ε_2 displayed a wavelength-dependent lifetime in the picosecond range corresponding to the energy dependent internal conversion rate of the dark S_1 keto state formed by the proton transfer.

the ground and excited state. These results suggest that interactions with a nearby $n\pi^*$ state may play an important role in the keto internal conversion. This example illustrates how TRPES can be used to study the dynamics of biologically relevant processes such as proton transfer, revealing details of both the proton transfer step and the subsequent dynamics in the "dark" state formed after the proton transfer.

4.2.2. *Photostability of DNA bases*

The UV photostability of the DNA bases is determined by the competition between a number of ultrafast excited-state electronic relaxation

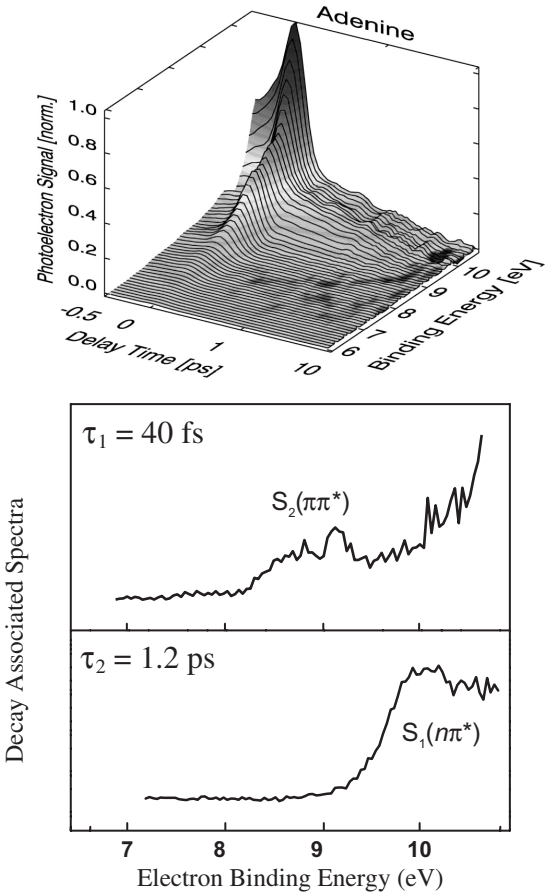

Fig. 6. Femtosecond TRPES spectra of adenine (top) recorded at 267 nm pump and 200 nm probe. The time axis is plotted on a logarithmic scale. The decay-associated spectra of the 40 fs and 1.2 ps channels, extracted from a biexponential global 2D fit, are shown (bottom). The 40 fs time constant spectrum corresponds to $\pi\pi^* \rightarrow D_0$ (π^{-1}) photoionization. The 1.2 ps time constant spectrum corresponds to $n\pi^* \rightarrow D_1$ (n^{-1}) photoionization. This confirms that the optically bright but short-lived $\pi\pi^*$ state decays via internal conversion to the dark but longer lived $n\pi^*$ state.

processes, some of which may be destructive to the molecule. In order to protect against these potentially harmful processes, nature designed ultrafast protective mechanisms that convert dangerous electronic energy to less dangerous vibrational energy. The purine base adenine is a heterocycle, having a strong $\pi\pi^*$ UV absorption band and, due to the lone electron pairs on the heteroatoms, has an additional low lying $n\pi^*$ state. In the

gas phase, the 9H tautomer of isolated adenine is the lowest energy and most abundant form. The relative importance of the electronic relaxation channels in adenine has been a matter of some debate.[71,72] A TRPES study of the excited-state decay dynamics of adenine at 267 nm excitation, shown in Fig. 6, required a biexponential fit using two time constants: a fast component decaying in 40 fs followed by a slower component with a 1.2 ps lifetime.[73] A broad photoelectron band in the 7.5–10.8 eV range decays quickly and transforms into a second band spanning the 8.5–10.8 eV range. This second band grows smoothly between 8.5–9.6 eV and then decays slowly. Beyond 6 ps, no remaining photoelectron signal was observed. The two lowest electronic states of the adenine cation are the D_0 (π^{-1}) cation ground state and the D_1 (n^{-1}) cation excited state. The expected Koopmans' correlations are: $\pi\pi^* \rightarrow D_0$ (π^{-1}) and $n\pi^* \rightarrow D_1$ (n^{-1}). The spectrum of the 40 fs component corresponds to the $\pi\pi^* \rightarrow D_0$ (π^{-1}) ionizing transition whereas that of the 1.1 ps component to the $n\pi^* \rightarrow D_1$ (n^{-1}) ionizing transition. These TRPES results confirm that, in adenine, the short-lived state formed upon UV photoexcitation is the $\pi\pi^*$ state, which, upon internal conversion, forms the longer lived $n\pi^*$ state, itself decaying back to the ground state. This ultrafast radiationless decay to the ground state represents therefore a rapid conversion of "dangerous" electronic energy to "less dangerous" vibrational energy, since the former may lead to photochemistry whereas the latter may be rapidly quenched by dissipation to the surrounding water solvent.

5. Concluding Remarks

The ability of time-resolved photoelectron spectroscopy to interrogate vibronic wavepackets on nonadiabatically coupled molecular potential energy surfaces presents an excellent opportunity to take advantage of the deep and growing relationship between experiment and theoretical simulation. The nature and quality of the information available from a well designed TRPES experiment can be directly comparable to the highly detailed predictions of *ab initio* computation. Through the exploitation of the tendency for different excited molecular electronic states to preferentially ionize into different continuum channels, on the dependence of observed Franck–Condon spectra on the motion of the nuclei, in the determination of molecular frame photoelectron angular distributions, and with time resolution on the order of femtoseconds, this spectroscopic technique

has the potential to achieve deep insights into the nature of excited state polyatomic molecular dynamics. In fact, insights that were, until recently, exclusively the domain of theoretical simulation may now be gleaned from experimental results.

The nature of this detailed interplay between theory and experiment has farther reaching implications than simply the employment of wavepacket simulations to aid in the explanation of experimental results or in the validation of a given level of theory. Rather, we believe that the correlated development of experimental and *ab initio* molecular dynamics methods will play a key role in developing simplified "rules" that govern the behavior of excited polyatomic molecules. It might be said that conical intersections play a role in excited state dynamics analogous to that of the transition state in ground state dynamics. For ground state reaction dynamics, the Polanyi rules relate the topographical features of the transition state to the outcomes and energy disposal of the reaction.[74] For example, ground state A + BC reactions with "late" transition state barriers are move favorably traversed by vibrationally excited BC reactants, as opposed to "early" barriers that are more favorably crossed by high velocity collisions. By analogy with the Polanyi rules, we might expect that specific vibrational dynamics at conical intersections will be as important to the dynamics as are the topographical feature of the conical intersection itself. We look forward to the experimental–theoretical developments of many research groups which will give birth to an unprecedentedly detailed picture of dynamical processes in polyatomic molecules.

Acknowledgments

We thank our co-workers and collaborators Prof. Todd J. Martinez, M. Z. Zgierski, S. Patchkovskii, A. Boguslavskiy, O. Schalk, P. Hockett, O. Clarkin and G. Wu for numerous insightful discussions.

References

1. M. Bixon and J. Jortner, *J. Chem. Phys.* **48**, 715 (1968).
2. J. Jortner, S.A. Rice and R.M. Hochstrasser, *Adv. Photochem.* **7**, 149 (1969).
3. S.R. Henry and W. Siebrand, in *Organic Molecular Photophysics*, edited by J.B. Birks (John Wiley & Sons, Inc., London, 1973), Vol. 1, pp. 152.

4. K.F. Freed, in *Radiationless Processes in Molecules and Condensed Phases*, edited by F.K. Fong (Spring-Verlag, Berlin, 1976), pp. 23.
5. G. Stock and W. Domcke, *Adv. Chem. Phys.* **100**, 1 (1997).
6. G.A. Worth and L.S. Cederbaum, *Annu. Rev. Phys. Chem.* **55**, 127 (2004).
7. M. Klessinger and J. Michl, *Excited States and Photochemistry of Organic Molecules*. (VCH, New York, 1994).
8. H. Köppel, W. Domcke and L.S. Cederbaum, *Adv. Chem. Phys.* **57**, 59 (1984).
9. M. Born and J.R. Oppenheimer, *Ann. Phys. (Leipzig)* **84**, 457 (1927).
10. G.J. Atchity, S.S. Xantheas and K. Ruedenberg, *J. Chem. Phys.* **95**, 1862 (1991).
11. D.R. Yarkony, *Acc. Chem. Res.* **31**, 511 (1998).
12. H. Köppel, W. Domcke and L.S. Cederbaum, in *Conical Intersections*, edited by W. Domcke, D.R. Yarkony and H. Koppel (World Scientific, New Jersey, 2004), Vol. 15, pp. 323.
13. A. Stolow, A. Bragg and D.M. Neumark, *Chem. Rev.* **104**, 1719 (2004).
14. I. Fischer, M. Vrakking, D. Villeneuve and A. Stolow, in *Femtosecond Chemistry*, edited by M. Chergui (World Scientific, Singapore, 1996).
15. A. Stolow, *Philos. Trans. R. Soc. Lodon, Ser. A.* **356**, 345 (1998).
16. C.C. Hayden and A. Stolow, in *Advanced Physical Chemistry*, edited by C.-Y. Ng (World Scientific, Singapore, 2000), Vol. 10.
17. W. Radloff, in *Advanced Physical Chemistry*, edited by C.-Y. Ng (World Scientific, Singapore, 2000), Vol. 10.
18. K. Takatsuka, Y. Arasaki, K. Wang and V. McKoy, *Faraday Discuss* **115**, 1 (2000).
19. D.M. Neumark, *Annu. Rev. Phys. Chem.* **52**, 255 (2001).
20. A. Stolow, *Annu. Rev. Phys. Chem.* **54**, 89 (2003).
21. A. Stolow, *Inter. Rev. Phys. Chem.* **22**, 377 (2003).
22. T. Suzuki, T. Seideman and M. Stener, *J. Chem. Phys.* **120**, 1172 (2004).
23. V. Wollenhaupt, M. Engel and T. Baumert, *Annu. Rev. Phys. Chem.* **56**, 25 (2005).
24. A. Stolow and J.G. Underwood, *Adv. Chem. Phys.* **139**, 497 (2008).
25. T. Suzuki, *Annu. Rev. Phys. Chem.* **57**, 555 (2006).
26. T. Seideman, *Annu. Rev. Phys. Chem.* **53**, 41 (2002).
27. L.S. Cederbaum, in *Conical Intersections*: *Electronic Structure, Dynamics and Spectroscopy*, edited by W. Domcke, D.R. Yarkony and H. Köppel (World Scientific, Singapore, 2004), Vol. 15, pp. 3.
28. T. Pacher, L.S. Cederbaum and H. Köppel, *Adv. Chem. Phys.* **84**, 293 (1993).
29. M. Born and K. Huang, *Dynamical Theory of Crystal Lattices*. (Oxford University Press, 1954).
30. D.R. Yarkony, in *Conical Intersections*: *Electronic Structure, Dynamics and Spectroscopy*, edited by W. Domcke, D.R. Yarkony and H. Köppel (World Scientific, Singapore, 2004), Vol. 15, pp. 41.
31. R. Renner, *Z. Phys.* **92**, 172 (1934).
32. C. Jungen and A.J. Merer, in *Modern Spectroscopy*: *Modern Research*, edited by K.N. Rao (Academic, New York, 1976), Vol. II.

33. H. Lischka, M. Dallos, P. Szalay, D.R. Yarkony and R. Shepard, *J. Chem. Phys.* **120**, 7322 (2004).
34. M. Dallos, H. Lischka, P. Szalay, R. Shepard and D.R. Yarkony, *J. Chem. Phys.* **120**, 7330 (2004).
35. J.F. Stanton and R.J. Bartlett, *J. Chem. Phys.* **98**, 7029 (1993).
36. A.I. Krylov, *Annu. Rev. Phys. Chem.* **59**, 433 (2008).
37. J.F. Stanton, *J. Chem. Phys.* **115**, 10382 (2001).
38. T. Ichino, A.J. Gianola, W.C. Lineberger and J.F. Stanton, *J. Chem. Phys.* **125**, 084312 (2006).
39. J.F. Stanton, *J. Chem. Phys.* **126**, 134309 (2007).
40. K.L. Reid, *Annu. Rev. Phys. Chem.* **54**, 397 (2003).
41. K. Wang and V. McKoy, *Annu. Rev. Phys. Chem.* **46**, 275 (1995).
42. Y. Arasaki, K. Takatsuka, K. Wang and V. McKoy, *J. Chem. Phys.* **112**, 8871 (2000).
43. R.R. Lucchese, *J. Electron Spectrosc. Relat. Phenom.* **141**, 201 (2004).
44. P. Hockett, M. Staniforth, K.L. Reid and D. Townsend, *Phys. Rev. Lett.* **102**, 253002 (2009).
45. V. Stert, W. Radloff, T. Freudenberg, F. Noack, I.V. Hertel, C. Jouvet, C. Dedonder-Lardeux and D. Solgadi, *Europhys. Lett.* **40**, 515 (1997).
46. V. Stert, W. Radloff, C.P. Schulz and I.V. Hertel, *Eur. Phys.* **5**, 97 (1999).
47. I.V. Hertel and W. Radloff, *Rep. Prog. Phys.* **69**, 1897 (2006).
48. B.T. Pickup, *Chem. Phys.* **19**, 193 (1977).
49. Y. Öhrn and G. Born, *Adv. Quantum Chem.* **13**, 1 (1981).
50. P. Langhoff, *Chem. Phys. Lett.* **22**, 60 (1973).
51. R.K. Nesbet, *Phys. Rev. A* **14**, 1065 (1976).
52. P. Langhoff, in *Electron-Molecule and Photon-Molecule Collisions*, edited by T. Rescigno, V. McKoy and B. Schneider (Plenum, New York, 1979), pp. 183.
53. K. Gokhberg, V. Vysotskiy, L.S. Cederbaum, L. Storchi, F. Tarantelli and V. Averbukh, *J. Chem. Phys.* **130**, 064104 (2009).
54. R.R. Lucchese, K. Takatsuka and V. McKoy, *Phys. Rep.* **131**, 147 (1986).
55. Y. Arasaki, K. Takatsuka, K. Wang and V. McKoy, *J. Chem. Phys.* **119**, 7913 (2003).
56. C.M. Oana and A.I. Krylov, *J. Chem. Phys.* **127**, 234106 (2007).
57. C.M. Oana and A.I. Krylov, *J. Chem. Phys.* **131**, 124114 (2009).
58. S. Patchkovskii, Z. Zhao, T. Brabec and D.M. Villenueve, *Phys. Rev. Lett.* **97**, 123003 (2006).
59. C. Jin, A.-T. Le, S.-F. Zhao, R.R. Lucchese and C.D. Lin, *Phys. Rev. A* **81**, 033421 (2010).
60. Y. Arasaki, K. Takatsuka, K. Wang and V. McKoy, *J. Chem. Phys.* **132**, 124307 (2010).
61. M. Seel and W. Domcke, *J. Chem. Phys.* **95**, 7806 (1991).
62. M. Seel and W. Domcke, *Chem. Phys.* **151**, 59 (1991).
63. V. Blanchet, M.Z. Zgierski and A. Stolow, *J. Chem. Phys.* **114**, 1194 (2001).
64. V. Blanchet, M.Z. Zgierski, T. Seideman and A. Stolow, *Nature* **401**, 52 (1999).
65. A. Warshel and M. Karplus, *Chem. Phys. Lett.* **17**, 7 (1972).

66. F. Zerbetto, M.Z. Zgierski, F. Negri and G. Orlandi, *J. Chem. Phys.* **89**, 3681 (1988).
67. M. Schmitt, S. Lochbrunner, J.P. Shaffer, J.J. Larsen, M.Z. Zgierski and A. Stolow, *J. Chem. Phys.* **114**, 1206 (2001).
68. E.V. Doktorov, I.A. Malkin and V.I. Man'ko, *J. Mol. Spec.* **64**, 302 (1977).
69. D. Gruner and P. Brumer, *Chem. Phys. Lett.* **138**, 310 (1987).
70. A. Hazra and M. Nooijen, *Int. J. Quant. Chem.* **95**, 643 (2003).
71. L. Serrano-Andrés, M. Merchán and A.C. Borin, *Proc. Natl. Acad. Sci. USA* **103**, 8691 (2006).
72. M. Barbatti and H. Lischka, *J. Am. Chem. Soc.* **130**, 6831 (2008).
73. C.Z. Bisgaard, H. Satzger, S. Ullrich and A. Stolow, *ChemPhysChem* **10**, 101 (2009).
74. J.C. Polanyi, *Acc. Chem. Res.* **5**, 161 (1972).